Encapsulating Fischer-Tropsch synthesis catalyst with porous graphite-carbon enables ultrahigh activity for syngas to α-olefins

Ke Wu [a], Zhenxuan Zhang [a], Ruoting Shan [a], Ling Li [a], Jungang Wang [b], Bo Hou [b], Yanfei Xu [a,c,*], Mingyue Ding [a,**]

[a] School of Power and Mechanical Engineering, Wuhan University, Wuhan 430072, China
[b] State Key Laboratory of Coal Conversion, Institute of Coal Chemistry, Chinese Academy of Sciences, Taiyuan 030001, China
[c] Suzhou Institute of Wuhan University, Suzhou 215125, China

ARTICLE INFO

ABSTRACT

Directly converting syngas to α-olefins via the Fischer-Tropsch synthesis reaction serves as a competitive alternative to the traditional petroleum route, which has attracted much recent attention. However, achieving high catalytic activity over the iron-based catalyst remains a grand challenge, due to the easy oxidation of the iron carbides active phase by the water produced during reaction. Herein, we present a porous graphite-carbon encapsulated iron-based catalyst, in which the iron carbides remain stable even under harsh reaction conditions of high CO conversion or high reaction temperature. Due to the excellent anti-oxidation ability of active phase, an ultrahigh activity for producing C_{4+} α-olefins of 11.35 $g \cdot g_{cat}^{-1} \cdot h^{-1}$ can be obtained. This work provides a promising strategy to develop iron-based Fischer-Tropsch synthesis catalysts with high catalytic activity and stability by rationally stabilizing iron carbides.

1. Introduction

Alpha-olefins (α-olefins), which contain terminal C=C bond, are important feedstocks in chemical industry. Among α-olefins, C_4, C_6 and C_8 are used as co-monomers in polyethylene products, C_5~C_{10} are used to manufacture plasticizers, C_{10}~C_{16} are used for the synthesis of surfactants, and C_{16}~C_{18} find their primary application as lubricating fluids [1–3]. Until now, α-olefins are mainly produced by ethylene oligomerization from the depleting petroleum resources, thus developing alternative routes to produce α-olefins is highly needed and promising. Recently, directly converting syngas (a mixture of CO and H_2) derived from renewable biomass, plentiful natural gas and coal into olefins has attracted an increasing research interest [4–8]. Fischer-Tropsch synthesis (FTS) is a classic reaction for the conversion of syngas to clean hydrocarbon fuels and value-added chemicals, and its reaction mechanism determines that it is easy to generate α-olefins [9].

Fe, Co, Ni and Ru are all catalytically active in the FTS reaction. Among them, the iron-based catalyst has great advantages in large-scale industrial applications, on account of its low price, wide operating conditions, and flexible hydrocarbons distribution [10,11]. Due to the

coexistence of H_2, CO, and H_2O during the FTS reaction, the Fe species can be reduced, carbonized, and oxidized with time on stream. As a result, the evolution of traditional iron-based catalyst generally resulted in a mixed phases of Fe_3O_4 and iron carbides under the FTS reaction conditions [12–14]. Iron carbides are recognized as the active sites for the activation of CO and the chain growth of hydrocarbons, while Fe_3O_4 is more active for the water-gas shift (WGS) side reaction (CO + H_2O ⇌ CO_2 + H_2) [15–17]. The oxidation of iron carbides into Fe_3O_4 limited the catalytic activity for producing hydrocarbons and led to a high selectivity of 40–50 % for the CO_2 by-product [18–20]. Therefore, synthesizing pure iron carbides as FTS catalyst and protecting it from oxidation are highly desirable.

Zhao et al. [21] successfully prepared pure-phase Fe, Fe_5C_2, Fe_2C, and Fe_7C_3 as the FTS catalysts. However, these iron carbides could be easily oxidized into Fe_3O_4 phase at CO conversion of about 25 %, leading to the gradually decrease of catalytic activity. Wang et al. [16] synthesized phase-pure Fe_2C catalyst by carefully controlling the pretreatment and carburization conditions, in which the Fe_2C phase could remain stable at 235 °C and CO conversion of 15 %. Many researchers have been devoted to enhance the catalytic activity and stability of iron carbides by

---

employing different promoters or supports. Gong et al. [22] found that Sn promoter could stabilize the iron carbide phase by promoting the removal of surface oxygen. However, Sn species easily migrated from bulk to surface and blocked the active sites of catalyst, leading to a lower catalytic activity. Cheng et al. [15] inhibited the formation of Fe_3O_4 phase by enhancing the carburization of Fe species via adding Mg and K promoters, whereas, the alkali metals promoter could cover the active sites and reduce the catalytic activity. Santos et al. [23] also reported a much lower catalytic activity and faster deactivation of iron-based catalyst after the addition of 1 % K promoter. In our previous work [24], we prepared an iron-based FTS catalyst encapsulated by hydrophobic SiO_2 shell, which could suppress the adsorption of H_2O and protect iron carbides from oxidation. However, at high CO conversion level (about 78 %), the amount of H_2O produced by the FTS reaction was high, and H_2O could still oxidize iron carbides into Fe_3O_4 before leaving the hydrophobic SiO_2. Stabilizing iron carbides at high CO conversion level to achieve high catalytic activity and stability is highly needed but remains a grand challenge.

The core@shell structure can play a variety of roles during the syngas conversion reaction and has attracted increasing attention recently. Xiao et al. [25] synthesized iron-based FTS catalyst coated with zeolite, in which the iron-based FTS catalyst and zeolite worked for converting syngas to hydrocarbons and secondary reforming of hydrocarbons, respectively. As a result, superior performance for syngas to gasoline was achieved on this zeolite-coated catalyst. Xu et al. [24] and Liu et al. [26] prepared iron-based FTS catalyst coated with hydrophobic SiO_2, which inhibited the adsorption of water on catalyst and hindered the side reactions related to water during syngas conversion. Zhang et al. [27] designed iron-based FTS catalyst coated with MnO_2, which accelerated the dissociation of CO and enhanced the production of C_{5+} long-chain hydrocarbons. Chen et al. [28] synthesized iron-based FTS catalyst coated with carbon nanotubes, and the confinement effect of carbon nanotubes significantly improved the reducibility of iron species and enhanced the yield of C_{5+} hydrocarbons. Ma et al. [29] prepared iron-based FTS catalyst coated with carbon shell, which facilitated the polymerization of light olefins and promoted the production of gasoline. Although many works have been done in the development of carbon-based catalysts for FTS [23,30,31], protecting iron carbides from oxidation based on the volume difference between different iron phases has rarely been reported.

Herein, we presented an iron-based FTS catalyst encapsulated by porous graphite-carbon, which could effectively avoid the sintering and oxidation of active Fe species. The iron carbide phase was stable under harsh reaction conditions, such as high CO conversion of 83 % or high reaction temperature of 330 °C. Due to the absence of Fe_3O_4 phase, an ultrahigh activity for producing hydrocarbons of 1450 $\mu mol_{CO} \cdot g_{Fe}^{-1} \cdot s^{-1}$ could be achieved, accompanied with a relatively low CO_2 selectivity of 29 %. Moreover, the space time yield (STY) for C_{4+} α-olefins reached 11.35 $g \cdot g_{cat}^{-1} \cdot h^{-1}$ after the addition of appropriate amount of Na promoter.

2. Experimental

2.1. Catalyst preparation

The graphite-carbon coated iron-based catalysts (Fe@GC) were synthesized by one-step melting and subsequent calcination processes. Typically, 3 g of glucose (AR) and 5 g of urea (AR) were vigorously stirred at 165 °C in a 100 mL beaker, which was fixed in an electric heating sleeve. Glucose and urea acted as carbon source and precipitating agent, respectively. After the solids melted completely into black liquid, 3.38 g of $Fe(NO_3)_3 \cdot 9 H_2O$ (AR) was added into the beaker. The mixture was vigorously stirred until it expanded and no new bubble was produced. Then, the mixture was heated at 180 °C for 24 h. Finally, the black product was calcined in a tube furnace under N_2 atmosphere (400 mL/min) at 400 °C for 30 min and then T °C (T = 550, 650, 750,

850) for 2 h, with a heating rate of 2 °C/min. The obtained catalysts were named as Fe@GC-T.

The Fe@GC catalysts with different iron contents (xFe@GC, x% was the mass content of iron in catalysts) were prepared by the same steps as Fe@GC-750 except that the dosage of $Fe(NO_3)_3 \cdot 9 H_2O$ was changed into 0.845 g, 1.69 g, 3.38 g, and 5.07 g, respectively.

The Fe@GC catalysts with different calcination times (Fe@GC-yh) were prepared by the same steps as Fe@GC-750 except that the obtained black product was calcined at 750 °C for 2 h, 4 h, and 8 h, respectively.

The Fe@GC-550–750 catalyst was prepared by the same steps as Fe@GC-T except for the calcination process. After one-step melting, the obtained black product was calcined in a tube furnace under N_2 atmosphere (400 mL/min) at 400 °C for 30 min, 550 °C for 2 h and then 750 °C for 2 h, with a heating rate of 2 °C/min.

Three kinds of iron-based catalysts without graphite-carbon coating were also prepared as the referring catalysts. The Fe@GC-550–750$_{air}$ catalyst was prepared by calcining Fe@GC-550 in air atmosphere at 750 °C for 2 h to burn off the surface graphite-carbon. Besides, two traditional Fe_2O_3 catalysts were prepared by the hydrothermal method. Typically, 15 g of $FeCl_3 \cdot 6 H_2O$ (AR) or 15 g of $Fe(NO_3)_3 \cdot 9 H_2O$ (AR) and 25 g of sodium acetate trihydrate (AR) were dissolved in 220 mL of water. Then, the black liquid was transferred into Teflon-lined stainless-steel autoclave and hydrothermally treated at 200 °C for 10 h. Finally, the obtained products were centrifuged, washed with water for four times, and dried at 100 °C for 12 h. The Fe_2O_3 catalysts synthesized with $FeCl_3 \cdot 6 H_2O$ and $Fe(NO_3)_3 \cdot 9 H_2O$ were denoted as Fe_2O_3-1 and Fe_2O_3-2, respectively.

The silicon dioxide coated iron-based catalyst ($Fe_2O_3@SiO_2$) was prepared by the modified Stöber method. Typically, 0.5 g of the above synthesized Fe_2O_3-1 was dispersed in 300 mL of ethanol (AR) by ultrasonication. Subsequently, 0.25 mL of tetraethoxysilane (AR) was added. After stirring for 3 h, 5 mL of ammonia (25 ~ 28 %, AR) and 20 mL of water were added. Then, the mixture was stirred for 24 h. Finally, the product was washed with ethanol and dried at 100 °C for 12 h.

$Fe_5C_2@SiO_2$ was prepared by treating the above synthesized $Fe_2O_3@SiO_2$ with reduction (400 °C, 0.1 MPa, 36 $L \cdot g_{Fe}^{-1} \cdot h^{-1}$, H_2, 24 h) and carbonization procedures (320 °C, 0.1 MPa, 36 $L \cdot g_{Fe}^{-1} \cdot h^{-1}$, H_2/CO = 2, 24 h).

$Fe_3O_4@SiO_2$ was obtained by further treating $Fe_5C_2@SiO_2$ with water vapor. During the water vapor treatment, liquid water with a flow rate of 0.005 mL/min was injected into the 31.6 %CO/68.4 %N_2 (10 mL/min) through a high pressure pump. This mixture containing liquid water was vaporized in a pre-heater at 300 °C. Then, the water vapor treatment was performed at 300 °C, 1.0 MPa for 20 h.

The Na-promoted catalysts (zNa/Fe@GC-550–750, z% was the mass content of Na in catalysts) were prepared by the impregnation method. Typically, 0.69 g of Fe@GC-550–750 and m g of Na_2CO_3 (AR) were added into 10 mL of water (m = 0.0163, 0.0899, and 0.1559, respectively). The mixture was dispersed by ultrasonication and then vigorously stirred at room temperature for 12 h. Subsequently, the mixture was heated at 50 °C until water was completely evaporated. Finally, the obtain solid was dried in a vacuum oven at 60 °C for 6 h.

2.2. Catalyst characterization

The powder X-ray diffraction (XRD) was performed on the Rigaku Ultima IV instrument. All the catalysts used Cu material as the target material, and the operating voltage and current were 40 kV and 40 mA, respectively. The catalysts were scanned at a rate of 10 °/min in the 2θ range of 5°~80°. The obtained XRD patterns were compared with the JCPDS standard cards to identify the phase composition.

X-ray photoelectron spectroscopy (XPS) measurements were performed on the ESCALAB250Xi instrument. The surface of sample was sputtered and etched with Ar ion to obtain the elements distribution along the depth of catalyst. All peaks were corrected by setting the C 1 s peak of 284.6 eV as the reference.

The surface morphology and elemental distribution of catalyst were characterized by scanning electron microscope (SEM) on the MIRA3 TESCAN microscope equipped with an Aztec Energy X-Max 20 energy dispersive X-ray spectroscopy (EDS) detector. Transmission electron microscope (TEM) images were obtained on the JEOL JEM 2100 F microscope with 200 kV accelerating voltage.

Nitrogen isothermal adsorption/desorption test was performed on the JWGB-BK100B instrument. The specific surface area of sample was analyzed by the Brunauer-Emmett-Teller (BET) method. Pore volume and pore size of sample were calculated by the Barrett-Joyner-Halenda (BJH) model. Before carrying the adsorption and desorption of N_2 at $-196\ ^\circ C$, all samples were pretreated under vacuum at $200\ ^\circ C$ for 4 h.

The Raman spectrum in the range of $100–2000\ cm^{-1}$ of catalyst was recorded on the XploRA Plus equipment with 532 nm laser condition. The thermogravimetric (TG) analysis was performed on the TGA2/DSC3, which was used to calculate the mass content of carbon and iron in catalyst. All catalysts were heated from $25\ ^\circ C$ to $900\ ^\circ C$ in air atmosphere with a heating rate of $10\ ^\circ C/min$.

2.3. Catalytic test

The syngas conversion was carried out in a fixed-bed reactor. Typically, 0.1 g of catalyst (40–80 mesh) was mixed with 0.1 g of quartz sand, and then packed into the reaction tube (diameter = 10 mm, length = 40 cm). Before each reaction, the catalyst was reduced at $350\ ^\circ C$ for 3 h in a pure H_2 flow (10 mL/min) at atmospheric pressure. After the reaction tube cooled to $200\ ^\circ C$, the syngas ($47.5\ \%CO/47.5\ \%H_2/5\ \%N_2$ or $31.6\ \%CO/63.4\ \%H_2/5\ \%N_2$) was fed into the reactor. The syngas conversion reactions were performed at $230–330\ ^\circ C$, 0.5–4.0 MPa, space velocity = $18–300\ L\cdot g^{-1}\cdot h^{-1}$, and the specific reaction conditions were indicated at the caption of each figure.

The reaction products during syngas conversion were separated via a hot trap ($70\ ^\circ C$) and a cold trap ($6\ ^\circ C$). The gaseous products were detected by the FULI GC 97 chromatograph equipped with a flame ionization detector (FID) and a thermal conductivity detector (TCD). RB-PLOT Al_2O_3 capillary column was connected to FID, while 5 A MolSieve and Porapak Q packed column were connected to TCD. Nitrogen was used as the internal standard, and methane correlated the data in TCD and FID. The liquid products, including the oil phase and aqueous phase products, were detected by another FULI GC 97 chromatograph equipped with two FID detectors (Figure S1). The oil products were separated by the RB-5 capillary column, and the molar number of each component was calculated based on the total mass of oil products and the proportion of each component in the chromatogram. The aqueous products were separated by the DB-FFAP capillary column, and the content of each component in water was calculated by adding acetone as the internal standard. Typically, 0.03 g of acetone was added to 0.1 g of aqueous products. The molar number of each component was calculated based on the total mass of aqueous products and the content of each component in water. The selectivity to oxygenates (methanol, ethanol, propanol) was
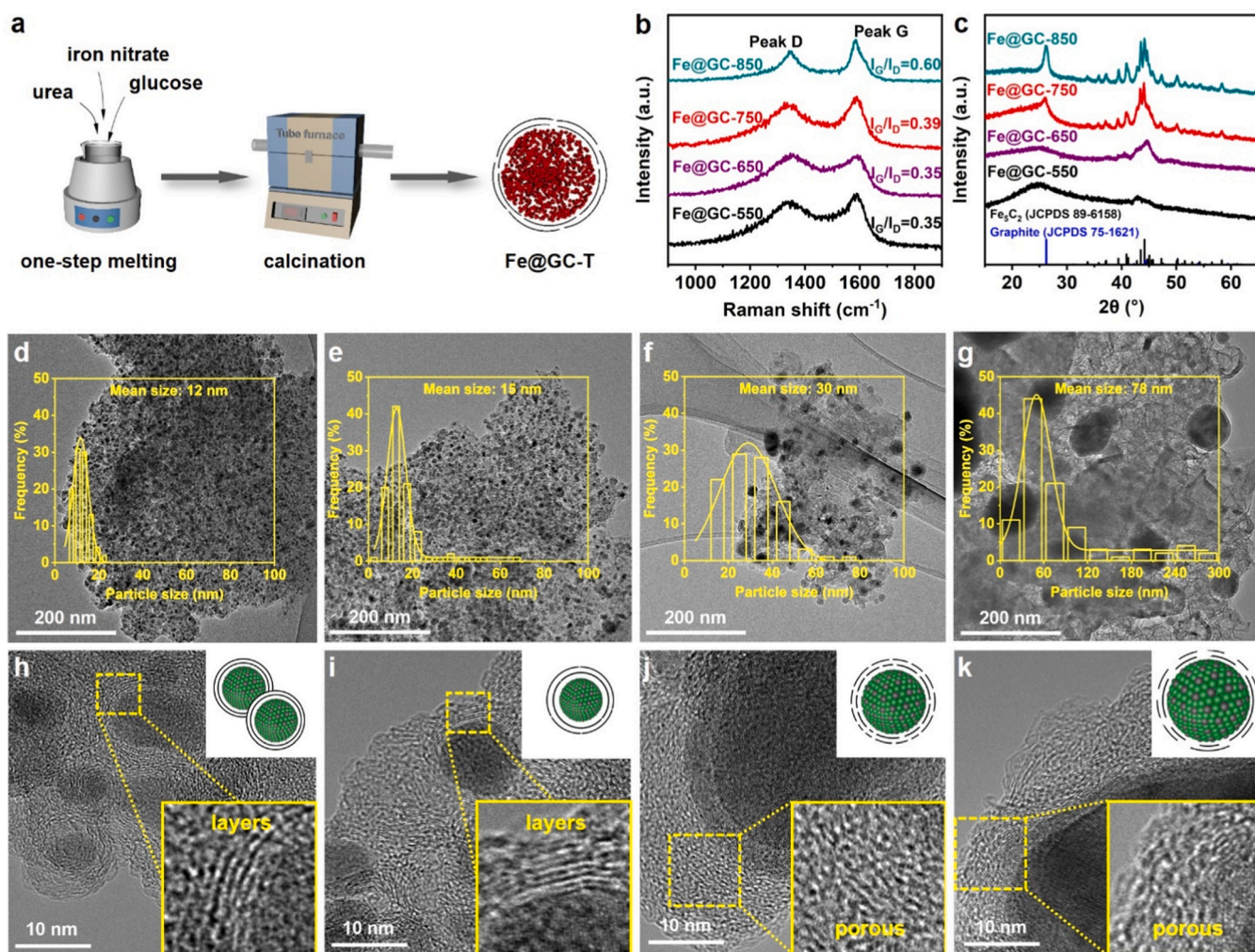

Fig. 1. (a) Synthesis steps of the Fe@GC-T catalysts. (b) Raman spectra and (c) XRD patterns of the spent Fe@GC-T catalysts. TEM and HRTEM images of the (d, h) spent Fe@GC-550, (e, i) spent Fe@GC-650, (f, j) spent Fe@GC-750, and (g, k) spent Fe@GC-850 catalysts.

less than 2 %C and was not reported in the product selectivity in detail below, since this work focused on the synthesis of hydrocarbon products. The CO conversion and hydrocarbons distribution were calculated based on carbon atom. The Fe-time yield (FTY) was defined as the moles of CO converted to hydrocarbons per gram of Fe per second. The carbon balance in each test was above 95 %.

3. Results and discussion

3.1. Structural characterization of Fe@GC-T

The graphite-carbon encapsulated iron-based catalysts (Fe@GC-T) were prepared by one-step melting and subsequent calcination at 550, 650, 750, and 850 °C, respectively (Fig. 1a). SEM images and relevant EDS elemental mapping suggested that Fe and C elements were dispersed homogeneously in the Fe@GC-T catalysts (Figure S2). The type and amount of carbon in the Fe@GC-T catalysts were further characterized by Raman spectra and TG technology. As shown in Figure S3, two peaks appeared at around 1360 cm^{-1} and 1587 cm^{-1} in the Raman spectra, which were attributed to the disordered (D type) and graphitic (G type) carbonaceous species, respectively [32]. The intensity ratio of G peak and D peak (I_G/I_D) reflected the graphitization degree of carbon materials. With the increase of calcination temperature, the I_G/I_D value gradually increased, suggesting that the graphitization degree of the carbon matrix in the Fe@GC-T catalysts was enhanced. The typical 2D peak appeared at around 2690 cm^{-1} also confirmed the formation of graphite-carbon in the Fe@GC-T catalysts. As shown in the TG curves (Figure S4), the slight weight loss below 200 °C and the obvious weight loss above 200 °C were attributed to the evaporation of adsorbed water and combustion of carbon matrix, respectively [33]. The weight-gain regions in the TG curves were attributed to the oxidation process of iron carbides into iron oxides in air. With the increase of calcination temperature, the total amount of carbon matrix in the Fe@GC-T catalysts slightly reduced, which was attributed to that high temperature could break the continuous layered structure of graphite-carbon (as discussed below in Fig. 1) and introduce more defects [34].

As shown in the TEM and HRTEM images (Fig. 1d to k), the iron nanoparticles were well encapsulated by the graphite-carbon shell with porous structure in all of the Fe@GC-T catalysts (Figure S5). Uniform and small iron nanoparticles (< 20 nm) could be obtained at the calcination temperature of 550 and 650 °C (Fig. 1d and e). The mean size of iron nanoparticles increased obviously from 12 nm of Fe@GC-550 to 78 nm of Fe@GC-850 (Fig. 1f and g), which was due to the stronger aggregation of iron species at higher calcination temperature. Besides, the calcination temperature obviously affected the continuity of graphite layers. The graphite layers of Fe@GC-550 and Fe@GC-650 were rather complete and continuous (Fig. 1h and i). With the increase of calcination temperature, large amounts of defects spread over the graphite layers of Fe@GC-750 and Fe@GC-850 (Fig. 1j and k), which could also be reflected by the increased pore volume (Figure S6 and Table S1). Combining the characterization results of TEM (Figure S7 and Fig. 1d-k), TG (Figure S4 and Figure S8), and Raman spectrum (Figure S3 and Fig. 1b) between the fresh and spent Fe@GC-T catalysts, it could be concluded that the structure, total amount and type of carbon matrix in catalysts were stable during reaction.

After reaction, only Fe$_5$C$_2$ phase was detected in the spent Fe@GC-750 and Fe@GC-850 catalyst (Fig. 1c), which was widely accepted as the most stable active phase for FTS. However, the diffraction peaks related to iron carbides in the spent Fe@GC-550 and Fe@GC-650 catalyst were very broad and weak. To illustrate the effect of the structure of graphite layers on the formation of active phase, we investigated the phase transformation of Fe@GC-550 and Fe@GC-750 during the reduction and reaction processes in detail (Figure S9). All the iron species in Fe@GC-550 and Fe@GC-750 were reduced into metallic iron by H$_2$ treatment. During further FTS reaction, the metallic iron in Fe@GC-750 could be completely carbonized, while almost no obvious

diffraction peak attributed to iron carbides was detected in Fe@GC-550. As discussed above (Fig. 1), the graphite layers of Fe@GC-550 were rather continuous, while many defects existed in the graphite layers of Fe@GC-750. These results demonstrated that the defects on graphite layers rendered channels for the diffusion of CO to internal iron species.

3.2. Optimization of catalyst structure

The synthesized Fe@GC-T catalysts were further applied to the FTS reaction. As discussed above, the calcination temperature of the Fe@GC-T catalysts simultaneously affected the particle size of iron species and the structure of graphite layers (Fig. 1 and Fig. 2a). The continuous and complete graphite layers coated on Fe@GC-550 restricted the diffusion and reaction of CO during syngas conversion, thus a low CO conversion was obtained (Figure S10). On the other hand, iron species obviously aggregated into large particles at high calcination temperature, which reduced the exposed active sites for syngas conversion, also leading to a low CO conversion over Fe@GC-850. As a result, the catalytic activity for producing hydrocarbons of the Fe@GC-T catalysts presented a volcanic curve with the increase of calcination temperature and reached the maximum value over Fe@GC-750 (Fig. 2b).

The iron loading in the Fe@GC-750 catalysts was adjusted by the dosage of iron nitrate and calcination time at 750 °C (Figures S11 to S17 and Table S2). With the increase of iron loading from 9 % to 38 %, CO conversion gradually increased due to the formation of more iron carbides active sites (Figure S18). However, as the further increase of iron loading, i.e., reduction in the content of graphite layers, CO conversion decreased rapidly, confirming the importance of graphite layers in enhancing the catalytic activity of catalyst. The effects of graphite layers on the phase composition and catalytic performance of catalyst were discussed in detail at Section 3.3 below.

The Fe@GC-550–750 catalyst was further synthesized by a two-step calcination process at 550 °C and then 750 °C. After the FTS reaction, the iron species in the Fe@GC-550–750 catalyst were converted into iron carbides without the formation of Fe$_3$O$_4$ phase (Fig. 2e). The elemental state on catalyst surface was further characterized by the XPS spectra combined with Ar ion etching (Fig. 2f). With the increase of etching time, the intensity of Fe 2p peaks obviously increased, suggesting that the graphite layers coated on iron species were gradually etched by the Ar ion treatment and the detection depth of XPS increased. Typical peaks at ca. 707.2/720.2 eV and 710.9/724.0 eV were detected (Fig. 2g), which were assigned to iron carbides and iron oxides, respectively [35–38]. Curve fitting of the Fe 2p spectrum indicated that the content of iron carbides in the surface layer of catalyst reached 86 %. Combining the analysis results of bulk structure by XRD and surface environment by XPS, the iron species in the spent Fe@GC-550–750 catalyst were presented in the form of iron carbides phase. The mean particle size of iron species in Fe@GC-550–750 was 18 nm, much smaller than that in Fe@GC-750 (Fig. 2c). Besides, compared with Fe@GC-550, more defects existed in the graphite layers of Fe@GC-550–750 (Fig. 2d). Thus, the catalytic activity for producing hydrocarbons of the Fe@GC-550–750 catalyst was much higher than the Fe@GC-550 and Fe@GC-750 catalysts (Fig. 2b).

3.3. Effect of graphite layer on the anti-oxidation ability of active phase

To illustrate the effect of graphite layers on the phase evolution behavior of iron species during the FTS reaction, the Fe@GC-550–750$_{air}$ catalyst was prepared, which was calcined in air to remove the graphite layers. TG curve and Raman spectrum verified the complete removal of graphite carbon shell (Figure S19). Besides, two traditional Fe$_2$O$_3$ catalysts were also synthesized by the hydrothermal method as referring catalysts (Figure S20).

During the FTS reaction, the Fe@GC-550–750$_{air}$ catalyst exhibited a low CO conversion of only 3 % (Fig. 3a), which was attributed to that the small iron species easily sintered and led to the deactivation of catalyst
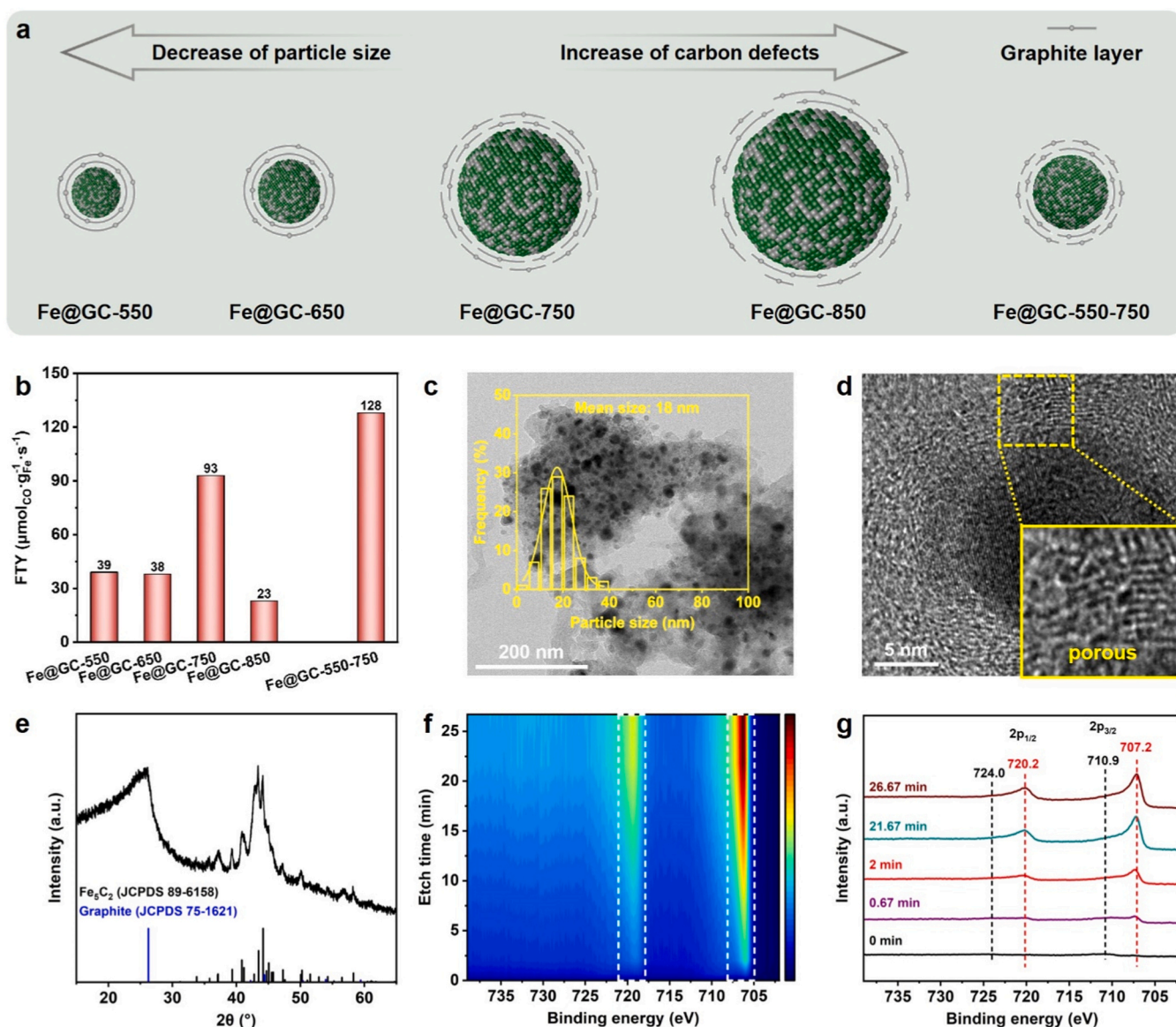
Fig. 2. (a) Structural model of the Fe@GC-T catalysts. (b) Catalytic activity for producing hydrocarbons of different catalysts. Reaction conditions: $H_2/CO = 1$, 300 °C, 1.0 MPa, space velocity = 18 $L \cdot g^{-1} \cdot h^{-1}$. (c) TEM image, (d) HRTEM image, and (e) XRD pattern of the spent Fe@GC-550–750 catalyst. (f, g) XPS spectra of the spent Fe@GC-550–750 catalyst during Ar ion etching.

[39,40]. By contrast, a high CO conversion of 83 % was achieved over the Fe@GC-550–750 catalyst, and the intrinsic activity for producing hydrocarbons of Fe@GC-550–750 was 42 times of that of Fe@GC-550–750$_{air}$ (Fig. 3b), demonstrating the importance of graphite layers in protecting the iron species from sintering. High CO conversion meant more H_2O was produced during the FTS reaction, and the iron carbides were generally oxidized by H_2O into Fe_3O_4 at CO conversion above 15 % [41–43]. Therefore, both Fe_3O_4 and iron carbides phases were detected in the spent Fe_2O_3 and Fe@GC-550–750$_{air}$ catalysts at CO conversion above 20 % (Fig. 3c). Interestingly, the iron species of the Fe@GC-550–750 catalyst still existed in the form of iron carbides phase even at high CO conversion level of 83 % (Fig. 2e to g).

In our previous work [44], we noticed that the core of iron-based catalyst shrank after the FTS reaction, implying that the spatial sizes of different iron phases were different and the phase transformation may lead to an obvious volume change of iron species. To further confirm this hypothesis, we prepared silicon dioxide coated iron-based catalysts (Fe@SiO$_2$) with Fe_5C_2 and Fe_3O_4 phases, respectively (Fig. 3d). In the Fe_5C_2@SiO$_2$ catalyst, there was large void between the Fe species and

SiO$_2$ shell (Fig. 3e). By treating Fe_5C_2@SiO$_2$ with water vapor, the Fe_5C_2 phase was converted completely into Fe_3O_4 phase. Little void was observed between the Fe species and SiO$_2$ shell in the Fe_3O_4@SiO$_2$ catalyst (Fig. 3f), confirming that Fe_3O_4 phase possessed much larger spatial size than Fe_5C_2 phase. This conclusion was also confirmed by the relative spatial size of different iron phases calculated based on the volume of unit cell (Figure S21). In other words, the oxidation of iron carbides into Fe_3O_4 was a volume-increasing process (Fig. 3g). In the Fe@GC-550–750 catalyst, the iron carbides were tightly confined by the graphite layers, which restricted the increase of iron particles and thus inhibited the oxidation of iron carbides (Fig. 3h). As a result, the iron carbides in the Fe@GC-550–750 catalyst remained stable during the FTS reaction. In summary, the graphite layers could effectively avoid the sintering and oxidation of active metal, thus leading to much higher catalytic activity for producing hydrocarbons (Fig. 3b). Besides, the graphite layers enhanced the C−C coupling ability of catalyst, facilitating the formation of long-chain hydrocarbons (Figure S22).
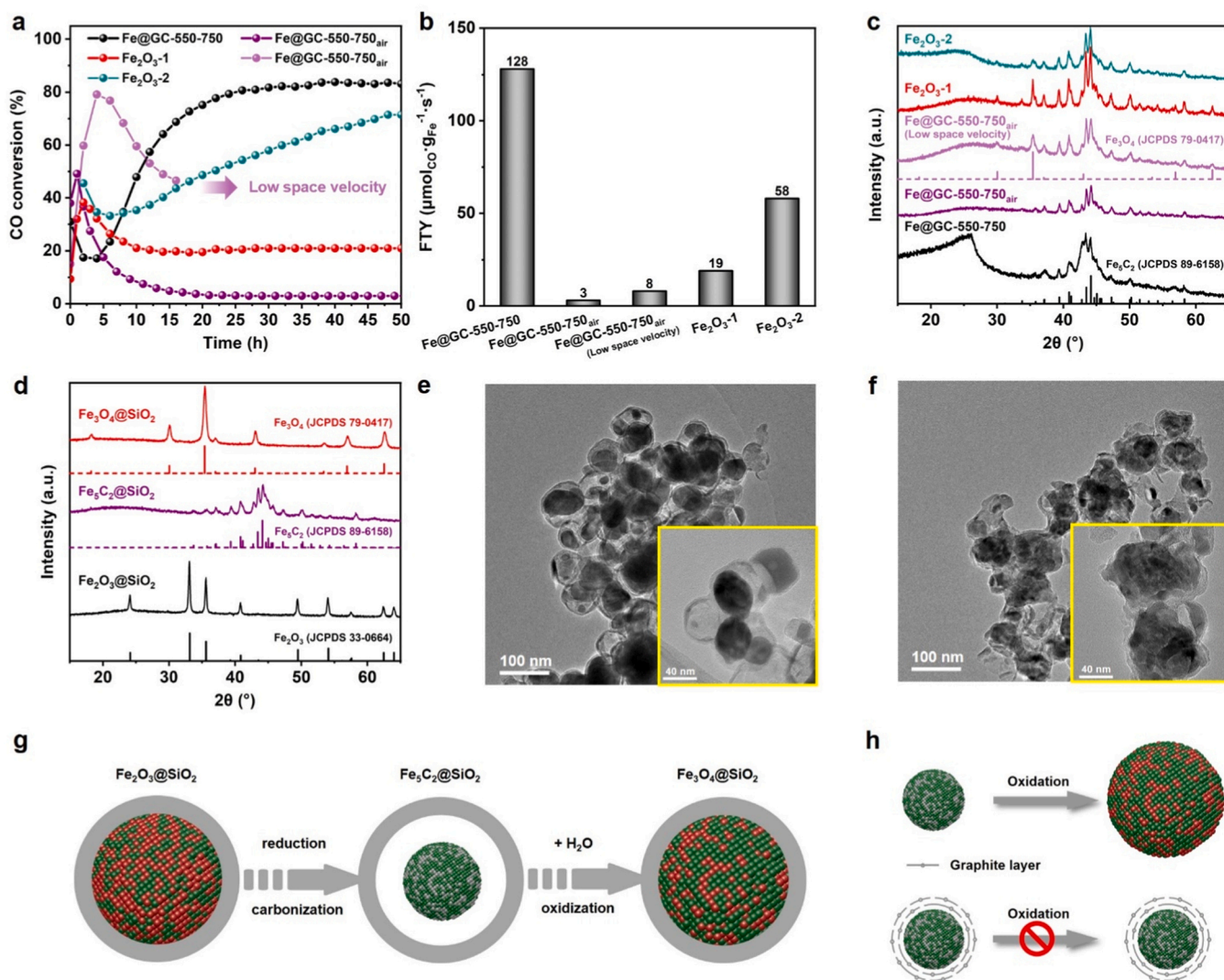
Fig. 3. (a) CO conversion and (b) catalytic activity for producing hydrocarbons of different catalysts. Reaction conditions: $H_2/CO = 1$, 300 °C, 1.0 MPa, space velocity = 18 $L \cdot g^{-1} \cdot h^{-1}$. Low space velocity = 3 $L \cdot g^{-1} \cdot h^{-1}$. (c) XRD patterns of the spent catalysts. (d) XRD patterns of $Fe_2O_3@SiO_2$, $Fe_5C_2@SiO_2$ and $Fe_3O_4@SiO_2$. TEM images of (e) $Fe_5C_2@SiO_2$ and (f) $Fe_3O_4@SiO_2$. (g) Structural model of the volume change of iron species during the carbonization and oxidation processes. (h) Anti-oxidation mechanism of the iron-based catalyst confined by graphite layers.

3.4. Ultrahigh activity for syngas to α-olefins

In addition to the intrinsic properties of catalyst, reaction conditions also affected the catalytic performance (Figure S23). Under the optimum reaction conditions, an ultrahigh FTY for producing hydrocarbons of 1450 $\mu mol_{CO} \cdot g_{Fe}^{-1} \cdot s^{-1}$ could be obtained over the Fe@GC-550–750 catalyst, which was much higher than the previous works (Fig. 4a and Table S3). We further tested the stability of the Fe@GC-550–750 catalyst (Fig. 4b). The FTY reached 1400 $\mu mol_{CO} \cdot g_{Fe}^{-1} \cdot s^{-1}$ after 20 h of reaction, and then remained around 1500 $\mu mol_{CO} \cdot g_{Fe}^{-1} \cdot s^{-1}$. The hydrocarbons selectivity was about 71 % with a CO_2 selectivity of 29 % during 72 h of continuous operation. Besides, the hydrocarbons distribution remained stable in reaction (Figure S24). In addition, the Fe_5C_2 phase was stable even at such harsh reaction conditions owing to the protection of graphite-carbon shell (Fig. 4c). Because Fe_3O_4 phase is the most active phase for the WGS reaction in the iron-based FTS catalysts [15–17], the absence of Fe_3O_4 phase in the Fe@GC-550–750 catalyst led to an obvious decrease of CO_2 selectivity from ~49% to 29% (Fig. 4a).

As for the hydrocarbons distribution, the Fe@GC-550–750 catalyst exhibited a high CH_4 selectivity of 38 % and a low olefins selectivity of only 33 % (Fig. 4d). After the addition of Na promoter, the CH_4 selectivity decreased obviously to 13 %, accompanied by the increase of chain growth probability (α value) from 0.50 over Fe@GC-550–750 to 0.71 over 8Na/Fe@GC-550–750 (Figure S25). Besides, Na enhanced the formation of olefins, especially the α-olefins (Figs. 4e to 4g). After the FTS reaction, the Fe species in the Na-promoted catalysts still existed in the form of iron carbide phase (Figure S26). On the other hand, Na facilitated the adsorption and conversion of CO, while excessive Na would cover the active sites and reduce the catalytic activity (Fig. 4h). The space time yield (STY) for C_{4+} α-olefins could reach 11.35 $g \cdot g_{cat}^{-1} \cdot h^{-1}$ over the 5Na/Fe@GC-550–750 catalyst, which was one order of magnitude higher than the maximum STY for total olefins or C_{2-4} light olefins reported in the previous studies through the FTS and Oxide-Zeolite (OX-ZEO) routes to the best of our knowledge (Fig. 4i and Table S4).

4. Conclusions

In summary, we have developed a strategy to stabilize iron carbides by the encapsulation of porous graphite-carbon. The oxidation of iron carbides into Fe_3O_4 is a volume-increasing process. In the Fe@GC catalysts, the iron carbides were tightly confined by the rigid graphite
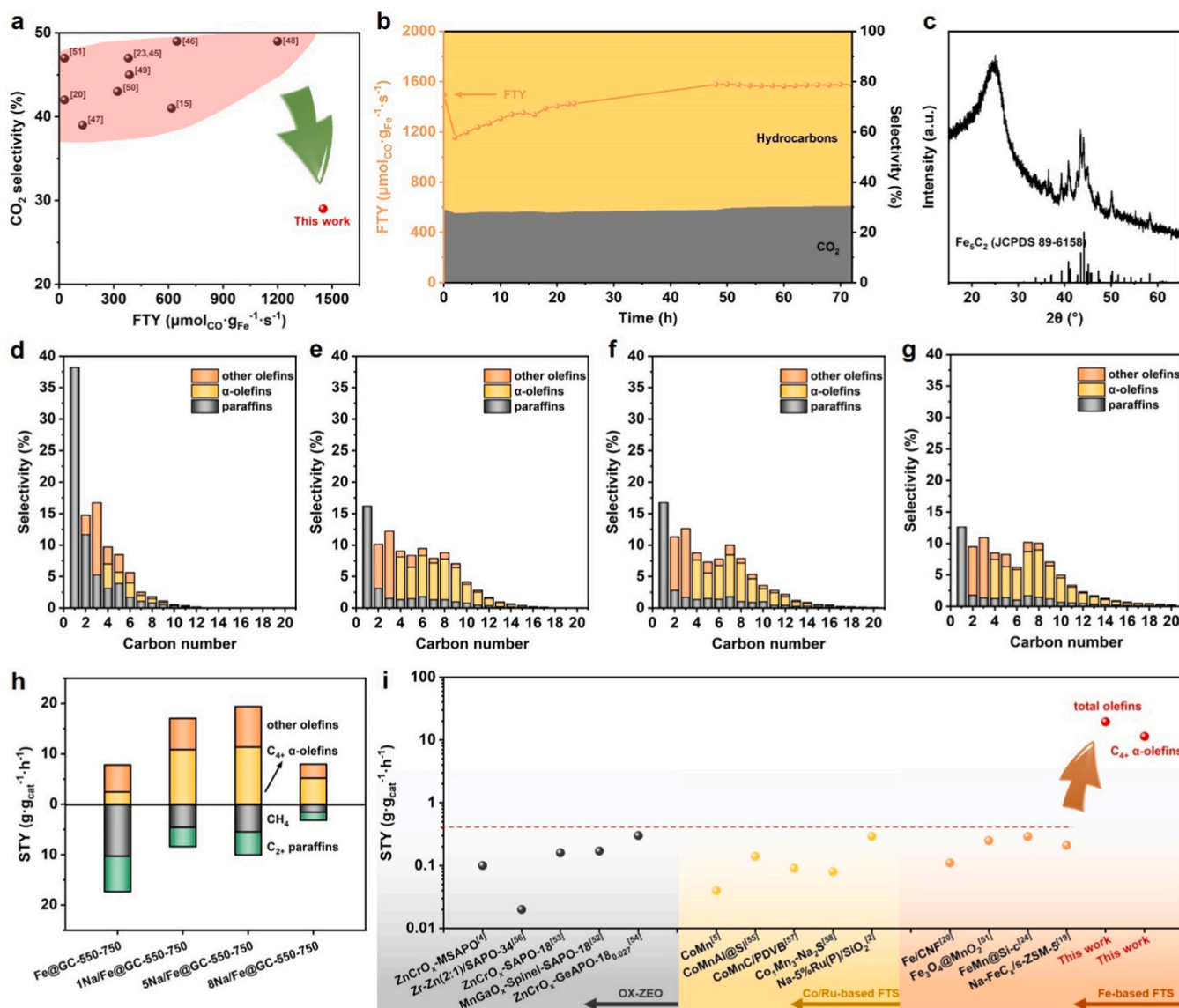
Fig. 4. (a) Comparison of catalytic activity for producing hydrocarbons with the previous works [15,20,23,45–51]. (b) Stability test for the Fe@GC-550–750 catalyst. Reaction conditions: $H_2/CO = 2$, 330 °C, 4.0 MPa, space velocity = 300 $L \cdot g^{-1} \cdot h^{-1}$. (c) XRD pattern of the Fe@GC-550–750 catalyst after stability test. Hydrocarbons distribution of the (d) Fe@GC-550–750, (e) 1Na/Fe@GC-550–750, (f) 5Na/Fe@GC-550–750, and (g) 8Na/Fe@GC-550–750 catalysts. (h) Space time yield for hydrocarbons of the Na/Fe@GC-550–750 catalysts. Reaction conditions: $H_2/CO = 2$, 330 °C, 4.0 MPa, space velocity = 300 $L \cdot g^{-1} \cdot h^{-1}$. (i) Comparison of space time yield for olefins of 5Na/Fe@GC-550–750 with the previous works [2,4,5,19,20,24,51–58].

layers, which restricted the increase of iron particles and thus inhibited the oxidation of iron carbides. The iron carbides were stable even under harsh reaction conditions, such as high CO conversion of 83 % or high reaction temperature of 330 °C. Due to the excellent anti-oxidation ability of active phase, the Fe_3O_4 phase was absent and an ultrahigh activity for producing C_{4+} α-olefins of 11.35 $g \cdot g_{cat}^{-1} \cdot h^{-1}$ could be obtained.

CRediT authorship contribution statement

Ling Li: Investigation. **Jungang Wang:** Resources. **Bo Hou:** Resources. **Yanfei Xu:** Writing – review & editing, Writing – original draft, Supervision, Project administration, Methodology, Investigation, Funding acquisition, Formal analysis, Conceptualization. **Mingyue Ding:** Writing – review & editing, Project administration, Funding acquisition. **Zhenxuan Zhang:** Investigation, Data curation. **Ruoting Shan:** Investigation. **Ke Wu:** Writing – original draft, Visualization, Validation, Resources, Methodology, Investigation, Formal analysis,

Data curation.

Declaration of Competing Interest

The authors declare that they have no known competing financial interests or personal relationships that could have appeared to influence the work reported in this paper.

Data Availability

Data will be made available on request.

Appendix A. Supporting information

Supplementary data associated with this article can be found in the online version at doi:10.1016/j.apcatb.2024.124067.

References

[1] J.C. Park, S. Jang, G.B. Rhim, J.H. Lee, H. Choi, H. Jeong, M.H. Youn, D. Lee, K. Y. Koo, S.W. Kang, J. Yang, H. Lee, H. Jung, C.S. Kim, D.H. Chun, A durable nanocatalyst of potassium-doped iron-carbide/alumina for significant production of linear alpha olefins via Fischer-Tropsch synthesis, Appl. Catal. A-Gen. 564 (2018) 190–198, https://doi.org/10.1016/j.apcata.2018.07.037.

[2] H. Yu, C. Wang, T. Lin, Y. An, Y. Wang, Q. Chang, F. Yu, Y. Wei, F. Sun, Z. Jiang, S. Li, Y. Sun, L. Zhong, Direct production of olefins from syngas with ultrahigh carbon efficiency, Nat. Commun. 13 (2022) 5987, https://doi.org/10.1038/s41467-022-33715-w.

[3] B. Gu, A.Y. Khodakov, V.V. Ordomsky, Selectivity shift from paraffins to α-olefins in low temperature Fischer-Tropsch synthesis in the presence of carboxylic acids, Chem. Commun. 54 (2018) 2345–2348, https://doi.org/10.1039/c7cc08692j.

[4] F. Jiao, J. Li, X. Pan, J. Xiao, H. Li, H. Ma, M. Wei, Y. Pan, Z. Zhou, M. Li, S. Miao, J. Li, Y. Zhu, D. Xiao, T. He, J. Yang, F. Qi, Q. Fu, X. Bao, Selective conversion of syngas to light olefins, Science 351 (2016) 1065–1068, https://doi.org/10.1126/science.aaf1835.

[5] L. Zhong, F. Yu, Y. An, Y. Zhao, Y. Sun, Z. Li, T. Lin, Y. Lin, X. Qi, Y. Dai, L. Gu, J. Hu, S. Jin, Q. Shen, H. Wang, Cobalt carbide nanoprisms for direct production of lower olefins from syngas, Nature 538 (2016) 84–87, https://doi.org/10.1038/nature19786.

[6] X. Pan, F. Jiao, D. Miao, X. Bao, Oxide-zeolite-based composite catalyst concept that enables syngas chemistry beyond Fischer-Tropsch synthesis, Chem. Rev. 121 (2021) 6588–6609, https://doi.org/10.1021/acs.chemrev.0c01012.

[7] Y. Liu, F. Lu, Y. Tang, M. Liu, F.F. Tao, Y. Zhang, Effects of initial crystal structure of Fe2O3 and Mn promoter on effective active phase for syngas to light olefins, Appl. Catal. B-Environ. 261 (2020) 118219, https://doi.org/10.1016/j.apcatb.2019.118219.

[8] S. Zhao, H. Li, B. Wang, X. Yang, Y. Peng, H. Du, Y. Zhang, D. Han, Z. Li, Recent advances on syngas conversion targeting light olefins, Fuel 321 (2022) 124124, https://doi.org/10.1016/j.fuel.2022.124124.

[9] E. de Smit, B.M. Weckhuysen, The renaissance of iron-based Fischer-Tropsch synthesis: on the multifaceted catalyst deactivation behaviour, Chem. Soc. Rev. 37 (2008) 2758–2781, https://doi.org/10.1039/b805427d.

[10] B.H. Davis, Fischer-Tropsch synthesis: relationship between iron catalyst composition and process variables, Catal. Today 84 (2003) 83–98, https://doi.org/10.1016/S0920-5861(03)00304-3.

[11] A. Demirbas, K. Dincer, Sustainable green diesel: a futuristic view, Energy Sources Part a-Recovery Util. Environ. Eff. 30 (2008) 1233–1241, https://doi.org/10.1080/15567030601082829.

[12] Q. Chang, C. Zhang, C. Liu, Y. Wei, A.V. Cheruvathur, A.I. Dugulan, J. W. Niemantsverdriet, X. Liu, Y. He, M. Qing, L. Zheng, Y. Yun, Y. Yang, Y. Li, Relationship between iron carbide phases (ε-Fe2C, Fe7C3, and χ-Fe5C2) and catalytic performances of Fe/SiO2 Fischer-Tropsch catalysts, ACS Catal. 8 (2018) 3304–3316, https://doi.org/10.1021/acscatal.7b04085.

[13] J. Zhang, M. Abbas, W. Zhao, J. Chen, Enhanced stability of a fused iron catalyst under realistic Fischer-Tropsch synthesis conditions: insights into the role of iron phases (χ-Fe5C2, θ-Fe3C and α-Fe), Catal. Sci. Technol. 12 (2022) 4217–4227, https://doi.org/10.1039/d2cy00703g.

[14] K.O. Otun, Y. Yao, X. Liu, D. Hildebrandt, Synthesis, structure, and performance of carbide phases in Fischer-Tropsch synthesis: a critical review, Fuel 296 (2021) 120689, https://doi.org/10.1016/j.fuel.2021.120689.

[15] Y. Cheng, J. Lin, T. Wu, H. Wang, S. Xie, Y. Pei, S. Yan, M. Qiao, B. Zong, Mg and K dual-decorated Fe-on-reduced graphene oxide for selective catalyzing CO hydrogenation to light olefins with mitigated CO2 emission and enhanced activity, Appl. Catal. B-Environ. 204 (2017) 475–485, https://doi.org/10.1016/j.apcatb.2016.11.058.

[16] P. Wang, W. Chen, F. Chiang, A.I. Dugulan, Y. Song, R. Pestman, K. Zhang, J. Yao, B. Feng, P. Miao, W. Xu, E.J.M. Hensen, Synthesis of stable and low-CO2 selective ε-iron carbide Fischer-Tropsch catalysts, Sci. Adv. 4 (2018) eaau2947, https://doi.org/10.1126/sciadv.aau2947.

[17] C. Pirola, C.L. Bianchi, A. Di Michele, P. Diodati, S. Vitali, V. Ragaini, Fischer Tropsch and water gas shift chemical regimes on supported iron-based catalysts at high metal loading, Catal. Commun. 10 (2009) 823–827, https://doi.org/10.1016/j.catcom.2008.12.006.

[18] J. Bai, C. Qin, Y. Xu, Di Xu, M. Ding, Preparation of nitrogen doped biochar-based iron catalyst for enhancing gasoline-range hydrocarbons production, ACS Appl. Mater. Interfaces 14 (2022) 45516–45525, https://doi.org/10.1021/acsami.2c14675.

[19] C. Wang, W. Fang, Z. Liu, L. Wang, Z. Liao, Y. Yang, H. Li, L. Liu, H. Zhou, X. Qin, S. Xu, X. Chu, Y. Wang, A. Zheng, F. Xiao, Fischer-Tropsch synthesis to olefins boosted by MFI zeolite nanosheets, Nat. Nanotechnol. 17 (2022) 714–720, https://doi.org/10.1038/s41565-022-01154-9.

[20] H.M.T. Galvis, J.H. Bitter, C.B. Khare, M. Ruitenbeek, A.I. Dugulan, K.P. de Jong, Supported iron nanoparticles as catalysts for sustainable production of lower olefins, Science 335 (2012) 835–838, https://doi.org/10.1126/science.1215614.

[21] H. Zhao, J. Liu, C. Yang, S. Yao, H. Su, Z. Gao, M. Dong, J. Wang, A. Rykov, J. Wang, Y. Hou, W. Li, D. Ma, Synthesis of iron-carbide nanoparticles: identification of the active phase and mechanism of Fe-based Fischer-Tropsch synthesis, CCS Chem. 3 (2021) 2712–2724, https://doi.org/10.31635/ccschem.020.202000555.

[22] H. Gong, H. Qing, H. Wan, X. Yuan, P. Qiao, X. Liu, X. Song, B. Wu, H. Wang, X. Wen, Y. Yang, Y. Li, Fe-Sn bimetallic catalysts for an enhanced Fischer-Tropsch synthesis stability via oxygen removal and coking resistance, Fuel 311 (2022) 122115, https://doi.org/10.1016/j.fuel.2021.122115.

[23] V.P. Santos, T.A. Wezendonk, J.J.D. Jaen, A.I. Dugulan, M.A. Nasalevich, H. Islam, A. Chojecki, S. Sartipi, X. Sun, A.A. Hakeem, A.C.J. Koeken, M. Ruitenbeek, T. Davidian, G.R. Meima, G. Sankar, F. Kapteijn, M. Makkee, J. Gascon, Metal organic framework-mediated synthesis of highly active and stable Fischer-Tropsch catalysts, Nat. Commun. 6 (2015) 6451, https://doi.org/10.1038/ncomms7451.

[24] Y. Xu, X. Li, J. Gao, J. Wang, G. Ma, X. Wen, Y. Yang, Y. Li, M. Ding, A hydrophobic FeMn@Si catalyst increases olefins from syngas by suppressing C1 by-products, Science 371 (2021) 610–613, https://doi.org/10.1126/science.abb3649.

[25] J. Xiao, K. Cheng, X. Xie, M. Wang, S. Xing, Y. Liu, T. Hartman, D. Fu, K. Bossers, M.A. van Huis, A. van Blaaderen, Y. Wang, B.M. Weckhuysen, Tandem catalysis with double-shelled hollow spheres, Nat. Mater. 21 (2022) 572–579, https://doi.org/10.1038/s41563-021-01183-0.

[26] X. Liu, T. Lin, P. Liu, L. Zhong, Hydrophobic interfaces regulate iron carbide phases and catalytic performance of FeZnOx nanoparticles for Fischer-Tropsch to olefins, Appl. Catal. B-Environ. 331 (2023) 122697, https://doi.org/10.1016/j.apcatb.2023.122697.

[27] Y. Zhang, L. Ma, T. Wang, X. Li, MnO2 coated Fe2O3 spindles designed for production of C5+ hydrocarbons in Fischer-Tropsch synthesis, Fuel 177 (2016) 197–205, https://doi.org/10.1016/j.fuel.2016.03.023.

[28] W. Chen, Z. Fan, X. Pan, X. Bao, Effect of confinement in carbon nanotubes on the activity of Fischer-Tropsch iron catalyst, J. Am. Chem. Soc. 130 (2008) 9414–9419, https://doi.org/10.1021/ja8008192.

[29] G. Ma, X. Wang, Y. Xu, Q. Wang, J. Wang, J. Lin, H. Wang, C. Dong, C. Zhang, M. Ding, Enhanced conversion of syngas to gasoline-range hydrocarbons over carbon encapsulated bimetallic FeMn nanoparticles, ACS Appl. Energ. Mater. 1 (2018) 4304–4312, https://doi.org/10.1021/acsaem.8b00932.

[30] Y. Chen, J. Wei, M.S. Duyar, V.V. Ordomsky, A.Y. Khodakov, J. Liu, Carbon-based catalysts for Fischer-Tropsch synthesis, Chem. Soc. Rev. 50 (2021) 2337–2366, https://doi.org/10.1039/d0cs00905a.

[31] Q. Zhang, J. Gu, J. Chen, S. Qiu, T. Wang, Facile fabrication of porous Fe@C nanohybrids from natural magnetite as excellent Fischer-Tropsch catalysts, Chem. Commun. 56 (2020) 4523–4526, https://doi.org/10.1039/d0cc01498b.

[32] L. Tang, X. Dong, W. Xu, L. He, A. Lu, Iron-based catalysts encapsulated by nitrogen-doped graphitic carbon for selective synthesis of liquid fuels through the Fischer-Tropsch process, Chin. J. Catal. 39 (2018) 1971–1979, https://doi.org/10.1016/S1872-2067(18)63158-4.

[33] S. Munir, M. Amin, N. Iqbal, A. Iqbal, A.A. Ghfar, Effect of pyrolysis on iron-metal organic frameworks (MOFs) to Fe3C@Fe5C2 for diesel production in Fischer-Tropsch synthesis, Front. Chem. 11 (2023) 1150565, https://doi.org/10.3389/fchem.2023.1150565.

[34] Y. Fang, J. Cao, X. Zhang, Y. Cao, N. Song, G. Qian, X. Zhou, X. Duan, Crucial roles of support modification and promoter introduction in Fe/CNT catalyzed syngas conversion to lower olefins, Catal. Today 368 (2021) 126–132, https://doi.org/10.1016/j.cattod.2020.02.024.

[35] C. Yang, H. Zhao, Y. Hou, D. Ma, Fe5C2 nanoparticles: a facile bromide-induced synthesis and as an active phase for Fischer-Tropsch synthesis, J. Am. Chem. Soc. 134 (2012) 15814–15821, https://doi.org/10.1021/ja305048p.

[36] Y. Chen, Z. Shi, Z. Wang, C. Wang, J. Feng, B. Pang, Q. Sun, L. Yu, L. Dong, Yolk-shell Fe@FeNx nanoparticles decorated N-doped mesoporous carbon as highly active electrocatalyst for oxygen reduction reactions, J. Alloy. Compd. 829 (2020) 154558, https://doi.org/10.1016/j.jallcom.2020.154558.

[37] Di Xu, H. Fan, K. Liu, G. Hou, C. Qin, Y. Xu, R. Li, J. Wang, M. Ding, Impacts of interaction between active components on catalyst deactivation over KFe/ZSM-5 bifunctional catalyst, ACS Sustain. Chem. Eng. 11 (2023) 10441–10452, https://doi.org/10.1021/acssuschemeng.3c01826.

[38] X. Liu, M. Xu, C. Cao, Z. Yang, J. Xu, Effects of zinc on χ-Fe5C2 for carbon dioxide hydrogenation to olefins: insights from experimental and density function theory calculations, Chin. J. Chem. Eng. 54 (2023) 206–214, https://doi.org/10.1016/j.cjche.2022.03.027.

[39] D. Weber, T. He, M. Wong, C. Moon, A. Zhang, N. Foley, N.J. Ramer, C. Zhang, Recent advances in the mitigation of the catalyst deactivation of CO2 hydrogenation to light olefins, Catalysts 11 (2021) 1447, https://doi.org/10.3390/catal11121447.

[40] X. Chen, D. Deng, X. Pan, X. Bao, Iron catalyst encapsulated in carbon nanotubes for CO hydrogenation to light olefins, Chin. J. Catal. 36 (2015) 1631–1637, https://doi.org/10.1016/S1872-2067(15)60882-8.

[41] K. Cheng, M. Virginie, V.V. Ordomsky, C. Cordier, P.A. Chernavskii, M.I. Ivantsov, S. Paul, Y. Wang, A.Y. Khodakov, Pore size effects in high-temperature Fischer-Tropsch synthesis over supported iron catalysts, J. Catal. 328 (2015) 139–150, https://doi.org/10.1016/j.jcat.2014.12.007.

[42] T.A. Wezendonk, X. Sun, A.I. Dugulan, A.J.F. van Hoof, E.J.M. Hensen, F. Kapteijn, J. Gascon, Controlled formation of iron carbides and their performance in Fischer-Tropsch synthesis, J. Catal. 362 (2018) 106–117, https://doi.org/10.1016/j.jcat.2018.03.034.

[43] W. Ning, N. Koizumi, H. Chang, T. Mochizuki, T. Itoh, M. Yamada, Phase transformation of unpromoted and promoted Fe catalysts and the formation of carbonaceous compounds during Fischer-Tropsch synthesis reaction, Appl. Catal. A-Gen. 312 (2006) 35–44, https://doi.org/10.1016/j.apcata.2006.06.025.

[44] Y. Xu, H. Liang, R. Li, Z. Zhang, C. Qin, D. Xu, H. Fan, B. Hou, J. Wang, X. Gu, M. Ding, Insights into the diffusion behaviors of water over hydrophilic/hydrophobic catalysts during the conversion of syngas to high-quality gasoline, Angew. Chem. Int. Ed. 62 (2023) e202306786, https://doi.org/10.1002/anie.202306786.

[45] T.A. Wezendonk, V.P. Santos, M.A. Nasalevich, Q.S.E. Warringa, A.I. Dugulan, A. Chojecki, A.C.J. Koeken, M. Ruitenbeek, G. Meima, H. Islam, G. Sankar, M. Makkee, F. Kapteijn, J. Gascon, Elucidating the nature of Fe species during pyrolysis of the Fe-BTC MOF into highly active and stable Fischer-Tropsch catalysts, ACS Catal. 6 (2016) 3236–3247, https://doi.org/10.1021/acscatal.6b00426.

[46] Y. Cheng, J. Lin, K. Xu, H. Wang, X. Yao, Y. Pei, S. Yan, M. Qiao, B. Zong, Fischer-Tropsch synthesis to lower olefins over potassium-promoted reduced graphene oxide supported iron catalysts, ACS Catal. 6 (2016) 389–399, https://doi.org/10.1021/acscatal.5b02024.

[47] C. Ma, W. Zhang, Q. Chang, X. Wang, H. Wang, H. Chen, Y. Wei, C. Zhang, H. Xiang, Y. Yang, Y. Li, θ-Fe₃C dominated Fe@C core-shell catalysts for Fischer-Tropsch synthesis: roles of θ-Fe₃C and carbon shell, J. Catal. 393 (2021) 238–246, https://doi.org/10.1016/j.jcat.2020.11.033.

[48] J. Bai, C. Qin, Y. Xu, Y. Du, G. Ma, M. Ding, Biosugarcane-based carbon support for high-performance iron-based Fischer-Tropsch synthesis, iScience 24 (2021) 102715, https://doi.org/10.1016/j.isci.2021.102715.

[49] S. Huang, C. Liu, Y. Chen, J. Hong, S. Lyu, Y. Zhao, Y. Zhang, J. Li, Organic-solvent assisted synthesis of highly dispersed iron based Fischer-Tropsch catalysts with MCF support: the effect of organic-solvent, Fuel 313 (2022) 122666, https://doi.org/10.1016/j.fuel.2021.122666.

[50] B. An, K. Cheng, C. Wang, Y. Wang, W. Lin, Pyrolysis of metal-organic frameworks to Fe₃O₄@Fe₅C₂ core-shell nanoparticles for Fischer-Tropsch synthesis, ACS Catal. 6 (2016) 3610–3618, https://doi.org/10.1021/acscatal.6b00464.

[51] J. Wang, Y. Xu, G. Ma, J. Lin, H. Wang, C. Zhang, M. Ding, Directly converting syngas to linear α-olefins over core-shell Fe₃O₄@MnO₂ catalysts, ACS Appl. Mater. Interfaces 10 (2018) 43578–43587, https://doi.org/10.1021/acsami.8b11820.

[52] B. Bai, C. Guo, F. Jiao, J. Xiao, Y. Ding, S. Qu, Y. Pan, X. Pan, X. Bao, Tuning the crystal phase to form MnGaOₓ -Spinel for highly efficient syngas to light olefins, Angew. Chem. Int. Ed. 62 (2023) e202217701, https://doi.org/10.1002/anie.202217701.

[53] G. Li, F. Jiao, X. Pan, N. Li, D. Miao, L. Li, X. Bao, Role of SAPO-18 acidity in direct syngas conversion to light olefins, ACS Catal. 10 (2020) 12370–12375, https://doi.org/10.1021/acscatal.0c03257.

[54] F. Jiao, B. Bai, G. Li, X. Pan, Y. Ye, S. Qu, C. Xu, J. Xiao, Z. Jia, W. Liu, T. Peng, Y. Ding, C. Liu, J. Li, X. Bao, Disentangling the activity-selectivity trade-off in catalytic conversion of syngas to light olefins, Science 380 (2023) 727–730, https://doi.org/10.1126/science.adg2491.

[55] T. Lin, P. Liu, K. Gong, Y. An, F. Yu, X. Wang, L. Zhong, Y. Sun, Designing silica-coated CoMn-based catalyst for Fischer-Tropsch synthesis to olefins with low CO₂ emission, Appl. Catal. B-Environ. 299 (2021) 120683, https://doi.org/10.1016/j.apcatb.2021.120683.

[56] K. Cheng, B. Gu, X. Liu, J. Kang, Q. Zhang, Y. Wang, Direct and highly selective conversion of synthesis gas into lower olefins: design of a bifunctional catalyst combining methanol synthesis and carbon-carbon coupling, Angew. Chem. Int. Ed. 55 (2016) 4725–4728, https://doi.org/10.1002/anie.201601208.

[57] W. Fang, C. Wang, Z. Liu, L. Wang, L. Liu, H. Li, S. Xu, A. Zheng, X. Qin, L. Liu, F. Xiao, Physical mixing of a catalyst and a hydrophobic polymer promotes CO hydrogenation through dehydration, Science 377 (2022) 406–410, https://doi.org/10.1126/science.abo0356.

[58] J. Xie, P.P. Paalanen, T.W. van Deelen, B.M. Weckhuysen, M.J. Louwerse, K.P. de Jong, Promoted cobalt metal catalysts suitable for the production of lower olefins from natural gas, Nat. Commun. 10 (2019) 167, https://doi.org/10.1038/s41467-018-08019-7.